A body in nonlinear near-wall shear flow: impacts, analysis and comparisons

Ryan A. Palmer[1]†, and Frank T. Smith[1]

[1]Department of Mathematics, University College London, London, WC1H 0AY, UK

(Received xx; revised xx; accepted xx)

Interaction between body motion and fluid motion is considered inside a nonlinear viscous wall layer, with this unsteady two-way coupling leading to impact of the body on the wall. The present paper involves a reduced system analysis which is shown to be consistent with computational solutions from direct numerical simulations for a basic flat-plate shape presented in an allied paper (Palmer & Smith 2020). The occurrence of impact depends mainly on fluid parameters and initial conditions. The body considered is translating upstream or downstream relative to the wall. Subsequent analysis focusses on the unusual nature of the impact at the leading edge. The impacting flow structure is found to have two nonlinear viscous-inviscid regions lying on either side of a small viscous region. The flow properties in the regions dictate the lift and torque which drive the body towards the wall. Pronounced flow separations are common as the impact then cuts off the mass flux in the gap between the body and the wall; here a nonlinear similarity solution sheds extra light on the separations. Comparisons are made between results from direct simulations and asymptotics at increased flow rate.

Key words: Impacts, analysis, fluid-body interaction, nonlinear dynamics, separation, near-wall, shear flow.

1. Introduction

Impact of a body onto a solid wall, following the travel of the body through a near-wall shear layer, is studied in the present work. The motion of the body and that of the surrounding fluid flow influence each other comparably and substantially. The motivations for the work concern aircraft safety especially when subjected to substantial disturbances due to ice crystals, ice lumps or other bodies in a boundary layer of air flow on a wing (Gent *et al.* 2000; Schmidt & Young 2009; Purvis & Smith 2016); such disturbances take many shapes and sizes but the case of a thin crystal is a fundamental one. There is also relevance to the transport of debris and dust in wider applications, to the movement of drugs or thrombi in blood vessel networks or lung airways, for example, and to atmospheric configurations.

Fluid dynamical issues of relevance centre on experimental and computational work on boundary layers, channel flows and related motions, instabilities, the attraction or repulsion between a body and a nearby wall, flow separations and previous work on solid-solid impacts, see Hall (1964); Einav & Lee (1973); Petrie *et al.* (1993); Portela *et al.* (2002); Poesio *et al.* (2006); Wang & Levy (2006); Yu *et al.* (2007); Schmidt & Young (2009); Loth & Dorgan (2009); Kishore & Gu (2010); Smith & Ellis (2010); Loisel

† Email address for correspondence: ryan.palmer.14@ucl.ac.uk

et al. (2013); Dehghan & Basirat Tabrizi (2014); Smith & Johnson (2016); Palmer & Smith (2019, 2020). The computational results in this last paper Palmer & Smith (2020) also highlight wake and upstream influence effects and the importance of scales as the local Reynolds number increases.

Concerning impacts and fluid-body interactions our aim is to understand more about the parametric effects and scales that govern the interactive behaviour. The recent findings of Smith & Johnson (2016); Smith (2017) suggest certain features in the linear regime. These focus on the effects from different lengths and locations of a body, thickness ratios and time scales. In general the effects act to destabilise the surrounding fluid motion, although several stabilising features are found, most notably from sufficient flexibility of the wall or the body or from slight streamwise movements of the body. The key parameters highlighted in these two papers include the density ratio between the body and the fluid, the characteristic Reynolds number, the fluctuation amplitude and the relative dimensions of the body compared with the typical flow thickness of the boundary layer or channel. The body shapes and initial conditions play a further significant role. Moreover the above raises interest in the nonlinear effects of a body moving upstream or downstream relative to a nearby fixed wall. The body of concern in the present work is a thin body, subjected to both viscous influences and nonlinear inertial influences from the surrounding fluid flow, and the work is intended to be complementary to direct simulations.

The paper deals with fluid-body coupling in a boundary layer or channel flow in particular for a relatively short body moving freely inside a viscous wall layer such that, in the normal direction, the thicknesses of the body and the wall layer are comparable cf. Smith & Palmer (2019). The effective Stokes number of the current interactions is assumed to be of order unity: in general the body disturbs the flow significantly, it does not follow the fluid particle paths closely as for a perfect tracer and it does not continue along its initial trajectory with ballistic behaviour. The typical Reynolds number is large however and so the near-wall behaviour is very sensitive within the viscous wall layer that arises. The representative Froude number is large and hence gravity is nominally negligible. In the context of an ice crystal within a boundary layer, the range of sizes of particles is of the order 10^{-3}m to 10^{-5}m. So the representative particle Reynolds number is 10^2 to 10^3 and the global Reynolds number may be 10^4 to 10^6, while the Froude number is of the order 10^6. Further details on icing conditions and the range of physical parameters are described in Norde (2017), Palmer & Smith (2019).

The interplay between body movement and fluid dynamics here thus has significant inertial and viscous components present along with fully nonlinear effects, which are able to provoke flow separations. The unsteadiness is another substantial component in the sense of the combined evolution of the fluid flow and the body position with time starting from an initial-value state. The major spatial scales involved are those of the viscous wall layer, but supplemented by those of a smaller adjustment zone which surrounds the leading edge of the thin body and adjusts the behaviour there in response to conditions downstream, while the major temporal scale is that of the body movement. The present interactions are considered for two spatial dimensions.

Here a fundamental problem is tackled concerning fluid-body interaction in the presence of an incident uniform shear flow close to a fixed wall. Section 2 describes the coupling that is induced for the laminar two-dimensional (2D) flow involving unsteady interactions with the body movement. So-called condensed flows, where interaction with the flow outside the viscous wall layer is negligible, are induced which are governed by the nonlinear boundary layer equations. To be specific, the main interactions are derived for the boundary layer on an airfoil, focussing on a relatively close-up view. Notably

however, the same problem holds for channel flow and for atmospheric boundary layers for example. The set-up here is for a general shape of body but then the emphasis is put on the fundamental case of the flat-plate body. Section 3 addresses the numerical solution of the central problem. Then sections 4 and 5 consider the resulting onsets of impact and related phenomena using analysis to complement numerical work and comparisons with the work of Palmer & Smith (2020). These onsets produce quite complex flow structure. Attention is given to the effects of a small velocity u_c of the body being positive, zero or negative relative to the wall, and the unknown scaled wall pressure and scaled wall shear stress or WSS are of interest throughout. Section 6 presents further discussion and conclusions.

2. The fluid-body coupling

In the boundary-layer scenario, fluid is flowing along an effectively flat surface, or wall, and far from the wall the free stream is moving with a given constant velocity parallel to that wall. This is locally on an airfoil surface, for example, or on a more general surface. The working below for the flow around a comparatively thin short body moving freely near the wall is expressed in terms of non-dimensional flow velocities (u, v), corresponding Cartesian coordinates (x, y), time t and pressure p, such that the dimensional versions are $\tilde{U}(u, v)$, $\tilde{L}(x, y)$, $\tilde{L}t/\tilde{U}$ and (to within an additive constant) $\tilde{\rho}\tilde{U}^2 p$ respectively. Here $\tilde{U}$ is the representative fluid velocity, taken to be the free-stream value, while $\tilde{L}$ is the airfoil chord, $\tilde{\rho}$ is the uniform density of the incompressible fluid and the temporal factor $\tilde{L}/\tilde{U}$ taken is the typical transport time. The velocity vector (u, v), pressure p and coordinates x, y are generally of order unity except near the wall which locally is positioned along the axis $y = 0$. In particular (u, v) is given by $(1, 0)$ in the far field and the leading edge of the airfoil is taken as the origin. The Reynolds number is given by $Re = \tilde{U}\tilde{L}/\tilde{\nu}$ where $\tilde{\nu}$ is the uniform kinematic viscosity of the fluid. The representative length of the body is ℓ which is $\tilde{\ell}/\tilde{L}$ and the primary concern is with the properties induced for a short body for which ℓ is small, when the Reynolds number is comparatively large. The body is generally translating upstream or downstream but only at a slow rate and so over the time scales of current interest the body is present at an effectively constant order-unity distance x_0 say downstream from the airfoil leading edge.

For large values of the Reynolds number Re, the thin boundary layer set up along the undisturbed surface ahead of the near-wall body and also downstream of it is a classical one having x scale of order unity. The y scale is of order $Re^{-1/2}$, with u, p variations of $O(1)$ and v being of $O(Re^{-1/2})$. The time scale there is of order unity. This boundary layer and its local free stream form the oncoming and surrounding flow field for the body/fluid interactive motion as in Figure 1. The main range of interest is for scaled lengths such that

$$Re^{-3/4} \ll \ell \ll Re^{-3/8}. \tag{2.1}$$

The range of validity in (2.1) (Smith 1976; Smith & Daniels 1981) is actually quite a large one in terms of the scales covered. Notably, the lower limit in (2.1) leads to a local problem governed by the full Navier-Stokes equations with very small $x - x_0$ and y values of order $Re^{-3/4}$ corresponding to a tiny particle. At the other extreme triple-deck theory applies. In between the two extremes, orders of magnitude show that a thin wall sublayer of thickness $O(l^{1/3}Re^{-1/2})$ is present (see Figures 1a, 1b) with typical pressure variation being of order $l^{2/3}$: the displacement of the flow just outside the boundary layer due to the dominant $O(l^{2/3})$ pressure variation inside the boundary layer is then of order $l^{5/3}$ and this is small compared with the sublayer thickness which is $O(l^{1/3}Re^{-1/2})$ provided

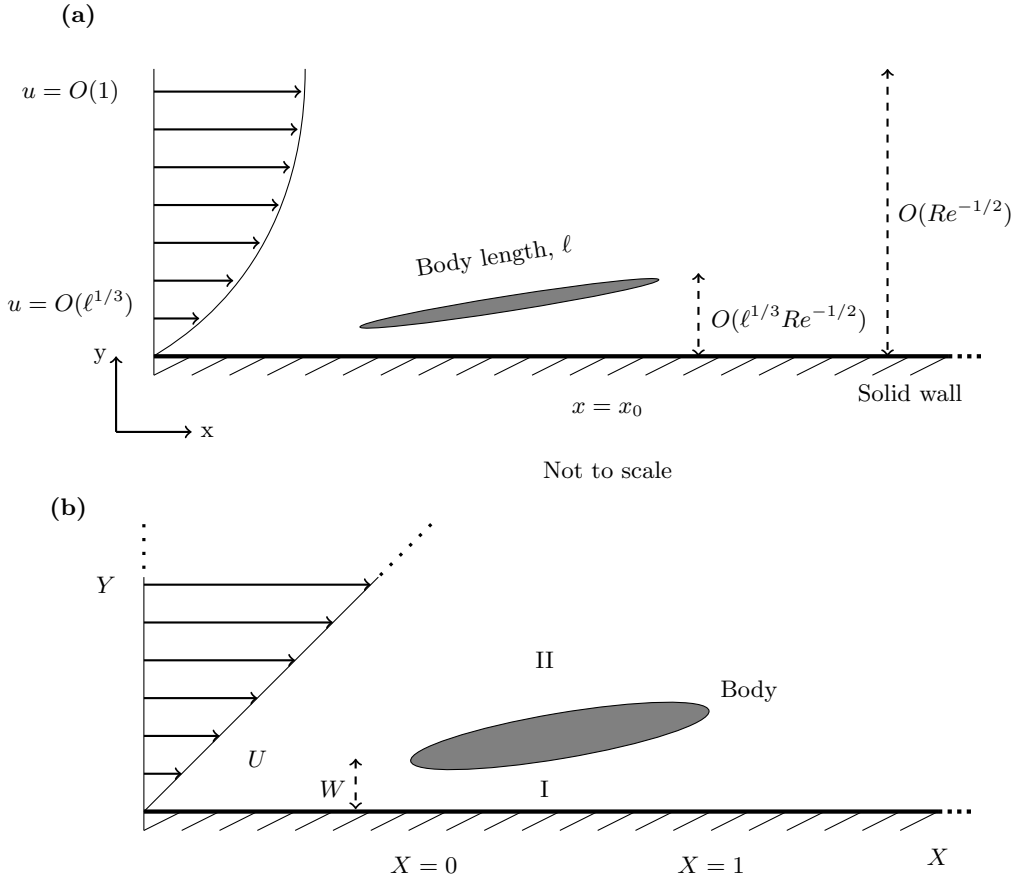

Figure 1: *(a, b) Sketch of the freely moving body within a viscous-inviscid wall layer and the resulting flow structure. The height W is the scaled normal distance from the straight wall to the leading edge of the body.*

$l \ll Re^{-3/8}$ as in (2.1). The flow structure for the range (2.1) is thus concentrated primarily in the thin sublayer surrounding the moving body as in Figures 1a and 1b. In the sublayer at leading order

$$(u, v, p) = \left(\ell^{1/3}U, \ell^{-1/3}Re^{-1/2}V, \ell^{2/3}P\right), \quad \text{with } x - x_0 = \ell X,\ y = \ell^{1/3}Re^{-1/2}Y,\ t = \alpha\ell^{2/3}T, \tag{2.2}$$

where the large constant α is to be determined and the capital-lettered quantities are of order unity. The body at an unknown position near the wall occupies the interval $0 < X < 1$ in a frame translating slowly streamwise with the body, with the body thickness being comparable with the sublayer height.

The Navier-Stokes equations then reduce to the quasi-steady condensed flow interaction (Smith 1976; Smith & Daniels 1981) in which:

$$U = \Psi_Y,\ V = -\Psi_X, \tag{2.3a}$$

$$UU_X + VU_Y = -P_X(X,T) + U_{YY}, \tag{2.3b}$$

within the gap I underneath the body and within the layer II above the body. Here Ψ is

the stream function. The unknown scaled pressure $P(X,T)$ is independent of Y because of the normal-momentum equation in each layer, such that:

$$P = P^+(X,T),\ P = P^-(X,T) \text{ above and below the body respectively.} \quad (2.3c)$$

The relevant boundary conditions are:

$$U = U_w,\ V = 0 \text{ at } Y = 0, \quad (2.4a)$$

$$U = V = 0 \text{ at } Y = F^-(X,T), \quad (2.4b)$$

$$(U,P) = \left(\lambda Y + U_w + a,\ \frac{U_w^2}{2} - \frac{(U_w+a)^2}{2}\right) \text{ at } X = 0^+. \quad (2.4c)$$

in the gap I. Herein the superscripts $+/-$ refer to the properties on top of and underneath the body in turn. The requirements (2.4a,b) stem from the no-slip conditions at the wall and on the moving under-surface F^- of the body. The effective streamwise velocity U_w of the wall is associated with the translation velocity u_c of the body relative to the wall: clearly if the body is translating upstream relative to the wall then U_w is positive. The conditions in (2.4c) are due to an unknown pressure jump arising across an Euler region (Smith *et al.* 2003) which surrounds the leading edge $X = 0$, with a corresponding jump $a = a(T)$ being induced in the streamwise velocity U to satisfy the quasi-steady Bernoulli balance. We should emphasize that the jump $a(T)$ is to be determined as part of the solution. The positive $O(1)$ factor λ in (2.4c) is the given scaled incident WSS, namely $Re^{-1/2}(\partial u/\partial y)$ at $y = 0$, in the surrounding boundary layer locally, as in Figures 1a and 1b but allowing here for the moving frame. The Euler region is similar to that in Smith *et al.* (2003); Jones & Smith (2003), its streamwise extent being of order $\ell^{1/3}Re^{-1/2}$. In summary, the physical need for the unknown pressure jump in (2.4c) at the leading edge stems from the upstream influence due to conditions at the trailing edge and mass conservation beneath the body. In the flow II on top of the body, by contrast, we have

$$U = V = 0 \text{ at } Y = F^+(X,T), \quad (2.5a)$$

$$U \sim \lambda Y + U_w \text{ as } Y \to \infty, \quad (2.5b)$$

$$(U,P) = (\lambda Y + U_w,\ \lambda a W) \text{ at } X = 0^+. \quad (2.5c)$$

The condition (2.5a) is for no slip on the top moving surface of the body. The function F^+ denotes the unknown scaled position of the body's top surface which is addressed further just below. The requirement (2.5b) of effectively zero displacement in Y corresponds to the feedback effect from the flow outside the sublayer being relatively small and is in keeping with the range specified in (2.1). Condition (2.5c) again comes from the Euler jump in pressure and in velocity, subject to mass conservation at the body surface and to the zero displacement associated with (2.5b); conservation of vorticity is assured because of the local λY variation throughout. The term W is the scaled width of the gap at, or the height of, the leading edge of the body and is in general an unknown function $W = W(T)$ of the scaled time.

We should comment additionally on certain features. The body, to repeat, is translating with a small constant velocity u_c which is assumed to be comparable with the fluid flow velocity in (2.2) and thus gives rise to the scaled wall velocity U_w in the moving frame, where $u_c = -\ell^{1/3}U_w$. Hence U_w can be positive or negative. The incident flow at $X = 0^-$ is one of constant shear with a velocity profile $U = \lambda Y + U_w$ for all $Y \geq 0$ and is at zero pressure. The different pressures P^+ and P^- induced above and below the body act to move the body as described below. The moving surface shapes F^+ and F^- are given

specifically by

$$F^{\pm}(X,T) = g^{\pm}(X) + h(T) + \left(X - \frac{1}{2}\right)\theta(T). \tag{2.6a}$$

Here $g^{\pm}(X)$ are the prescribed solid body shapes, atop and underneath, independent of T, whereas $h(T)$, $\theta(T)$ account for the evolving normal height and azimuthal rotation of the midpoint of the body. We deal with non-blunt bodies in the sense that $g^{\pm}$ are equal at $X = 0$, and can be set to zero there without loss of generality; hence $F^{\pm}$ are equal there, leading to the relation

$$W(T) = h(T) - \frac{1}{2}\theta(T), \tag{2.6b}$$

between W, h and θ. Along with this the values $g^{\pm}$ are taken to be equal at the trailing edge $X = 1$. Further, given that Ψ is zero at the wall, we note also the value

$$\Psi = \frac{\lambda W^2}{2} + (U_w + a)W \tag{2.6c}$$

holds for all $0 < X < 1$ at the under- and top-surfaces of the body from integration of (2.4c) across the gap. This value can also be used with (2.4c), (2.5c) to set the value of the stream function for all Y values at $X = 0^+$. Finally the condition

$$P^+ = P^- \text{ at } X = 1. \tag{2.6d}$$

applies since there can be no pressure difference across the wake behind the body and a Kutta condition of smooth departure of the flow from the trailing edge is imposed.

The body moves as it responds to the surrounding fluid flow via the differential pressure forcing at the top and under surfaces of the body. The body motion is controlled by:

$$M h_{TT} = \int_0^1 \left(P^-(X,T) - P^+(X,T)\right) dX (= C_L), \tag{2.7a}$$

$$J\theta_{TT} = \int_0^1 \left(X - \frac{1}{2}\right)\left(P^-(X,T) - P^+(X,T)\right) dX (= C_M), \tag{2.7b}$$

owing to the rates of change in the normal and angular momenta of the body. The mass $\tilde{M}$ of the body is equal to $\alpha^2\tilde{\rho}\tilde{L}^2\ell^{8/3}Re^{1/2}M$ with M being of order unity, and likewise the scaled moment of inertia J is $O(1)$. The centre of mass is taken as fixed at $X = 1/2$, which is a main case associated with a body of uniform density and any shape lengthwise symmetrical about the midpoint for example. The overall time scale is based on the body motion. As an estimate $\tilde{M}$ is approximately $\tilde{\rho}_B\tilde{V}$ in 2D where $\tilde{\rho}_B$ is the density of the body and the effective cross-sectional area $\tilde{V}$ is the product of the x and y scales in (2.2) multiplied by $\tilde{L}^2$ through non-dimensionalisation. Hence α^2 is comparable with $Re^{-1}\ell^{-4/3}\tilde{\rho}_B/\tilde{\rho}$. This means that the flow behaviour remains quasi-steady provided the density ratio $\tilde{\rho}_B/\tilde{\rho} \gg Re\ \ell^{4/3}$. Since the length ℓ is $O(Re^{-m})$ where $3/8 < m < 3/4$ from (2.1), the density ratio must exceed Re^n where $0 < n < 1/2$ (here n is $1 - 4m/3$) and so the theory is valid over a wide range of density ratios. Further in (2.7a,b) the P^+ and P^- responses are those produced by the fluid flow as described in (2.3a)-(2.6d), thus provoking fluid-body interaction. In the streamwise direction the body momentum and the relatively small fluid-flow forces are consistent with the body velocity u_c and hence the relative wall velocity U_w being constant as assumed earlier.

The central problem of the current fluid-body interaction is to solve (2.3a)-(2.7b). This is a nonlinear near-wall coupling which involves effects from viscous and inviscid dynamics. Our concern is with W being of order unity as opposed to the range of large

W values considered by Palmer & Smith (2019). The argument has been presented for a boundary-layer setting. A similar setting holds for channel flow and yields the same problem, with scale ranges being different from (2.1) and showing that to leading order there is no influence from the opposite wall of the channel. The interaction can also be expressed more broadly in terms of the local incident shear value alone.The present paper addresses numerical and analytical properties for a flat-plate body in the next two sections.

3. Numerical method and solutions

The numerical work used finite differencing based on a semi-implicit scheme for the two boundary-layer calculations required at each time step. At each X station the scheme iterates for the $P^{\pm}$ values in order to satisfy all the boundary conditions in the normal direction. A two-stepping procedure as in Smith & Timoshin (1996) is adopted to achieve second order accuracy. In the normal direction we transformed $\eta = Y/F^{-}$ in the fluid-filled gap region I and $\bar{Y} = Y - F^{+}$ in the region II on top of the body. In each region analysis for small positive X indicates that Blasius-like sublayers arise on each solid surface, thus occurring at the wall and at the underbody and overbody surfaces. The scheme coped satisfactorily with these irregularities by means of a transformation $X \to X^{1/2}$ to render all the sublayer normal coordinates linear in the transformed X coordinate and a sufficiently fine normal discrete step $\delta\eta$ or $\delta\bar{Y}$ to capture the Blasius-like local forms. Concerning streamwise marching the scheme in essence guessed the value of the slip jump a, marched forward successively in X and iterated on the a value in order to meet the Kutta requirement. The scheme sets the small spatial steps δX, $\delta\eta$ or $\delta\bar{Y}$ and temporal step δT such that typically 401 points were used in the streamwise direction, 401 normally and the time step was 0.001 or of that order. The uppermost boundary condition was placed at a $\bar{Y}$ value of 10 typically, while the marching in X extended from zero to unity: the latter is discussed further below. Finite grid effects were tested by varying these steps and placements and examining the changes to the solutions obtained, indicating that the results shown here are accurate to within a 1% error in pressure typically. The time-marching of the body-movement equations was discretised as an Euler procedure.

The work focusses on the flat plate as a central case, for which $g^{\pm}(X)$ are zero. Solutions are presented in Figure 2(a-g). The initial conditions have $(h, dh/dT, \theta, d\theta/dT)$ equal to $(2.5, -2, 1, 0)$, so the leading gap width $W = 2$ initially, while the moving wall velocity $U_w = 2$ and $(M, J) = (2, 0.3)$. Here by definition J cannot exceed $M/4$ but otherwise M, J have arbitrary positive values and we chose to use representative order-unity values as mentioned. In Figure 2(a) the movement of the flat-plate body is shown for successive scaled times T from 0.1 to 0.7. The body's inclination increases slightly as the body moves towards the wall and the leading edge impacts upon the wall (or rather is on the verge of impact) at a termination time of approximately 0.72. The corresponding development of W, a, θ with time is displayed in Figure 2(b) which confirms the gap closure as W tends to zero at termination. The slip value a is initially positive, then decreases to a small negative minimum and approaches a value close to zero at termination. The angle θ increases throughout, finishing with a value of about 1.25 at termination. Figure 2(c) presents the evolution of the scaled WSS ($\tau_g = \partial U/\partial Y$ at $Y = 0$) at the wall; eventually this becomes negative especially near the termination time at smaller X values but owing to the moving wall there is no flow reversal near the wall. Instead flow reversal takes place at the underbody prior to impact as indicated by the WSS ($\tau_b = -\partial U/\partial Y$ at $Y = F^{-}(X, T)$) there which is plotted in Figure 2(d) at successive times. The implied

separation here is relatively benign at first (it was treated by a Flare approach (Anderson *et al.* 2016), see also Figure 2(e,f)), it first occurs at the trailing edge just before a time T of 0.6 and it then spreads forward along the underbody, reaching an X station of about 0.15 at time 0.7. The corresponding pressure gradient produced is initially favourable over the entire underbody chord as inferred from the plots of the pressure $P = P^-$ in Figure 2(g). The growth of the Blasius-like layers near the leading edge tends to constrict the incoming flow and hence provoke a favourable pressure gradient anyway at small X, for all times. At later times however the gradient becomes adverse along much of the gap region as the separation region grows. The region of favourable gradient is pushed much closer to the leading edge. Overall, the pressure P^- at the opening position $X = 0^+$ remains negative but increasing for most of the evolution, in agreement with (2.4c), as $a(T)$ reduces, whereas eventually when $a(T)$ becomes negative P^- becomes positive. At the onset of impact when $a(T)$ tends to zero from below and $W(T)$ from above, P^- at the opening tends to zero from above, while a spatially rapid decrease in pressure also enters play near the opening then because of the approaching separation, generating a considerable favourable pressure gradient nearby followed by milder adverse pressure gradient. The velocity profiles at two streamwise stations $X = 0.06, 0.24$ are sampled at successive times in Figures 2(e,f) and they support the appearance of flow reversal near the underbody at later times prior to impact. The separation is relatively mild initially but then grows. The results also highlight the undeveloped nature of the flow at the smaller X values for earlier times compared with the well-developed forms at subsequent stations.

The flat-plate configuration studied here leads apparently to impact on the wall taking place at the leading edge of the body, at some finite termination time $T = T_0^-$. The computations become more difficult near termination because of small length scales appearing as well as increased separation, an aspect which points to the use of analysis near the termination time. The analytical investigation immediately below is into leading-edge impact (although we remark that for the present flat-plate body the impact might readily occur instead at the trailing edge).

4. Leading-edge impact

Guided by the above numerical solutions which indicate the onset of impact at the leading edge, we address analytically the behaviour when the width W of the gap I at the leading edge becomes small, as time $T \to T_0^-$. Due to the nature of the interaction, the treatment of steady flow is considered first and the relation to unsteady effects is then covered in full towards the end of the section. Moreover, to leading order the flow solution in layer II on top of the body remains finite.

4.1. *Impacting flow structure for upstream-moving bodies*

Assuming that U_w is $O(1)$ and positive, we note that on the body surface $\Psi = \Psi_0 = (a + U_w)W + \lambda W^2/2$, while the initial velocity profile in the gap is $U(X = 0^+, Y) = U_0 = a + U_w + \lambda Y$ and the initial pressure $P = P^-$ there is $P(X = 0^+) = P_0 = U_w^2/2 - (a + U_w)^2/2$. To deal with more general shapes (this is readily done analytically here) we can take the terminal (impacting) underbody shape $F^-(X, T_0)$ as any function $F(X)$ that is reasonably smooth with $F(0) = W$ nonzero, $F(X)$ positive (and of order W at least) for all X between 0 and 1, and $F(X)$ increasing to $O(1)$ for X of $O(1)$. A specific shape here is given by $F(X) = W + \gamma X^n$, with the power $n > 1/2$; the flat plate has n equal to unity. A solution is sought for the onset-of-impact situation where the initial gap height W becomes small. For $W \ll 1$ we may expect the unknown velocity

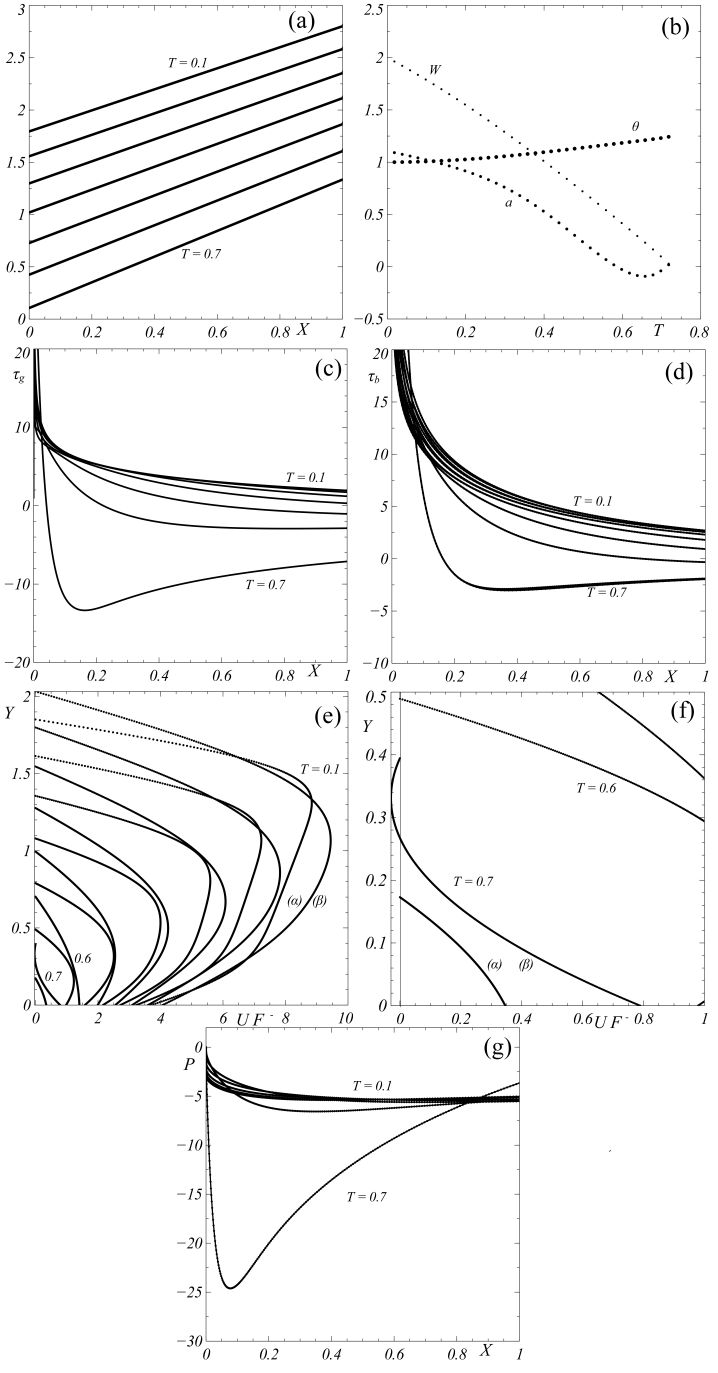

Figure 2: Results for flat-plate (straight) body. **(a)** Moving body configuration at scaled times T between 0.1 and 0.7. **(b)** Evolution of scaled height $W(T)$, orientation angle $\theta(T)$ and streamwise velocity jump $a(T)$. **(c)** Scaled wall shear stress (WSS) τ_g vs X at increasing T. **(d)** As (c) but for τ_b, the underbody surface shear stress. **(e)** Velocity profiles $F^{-}U$ at X values of 0.06 (α) and 0.24 (β) as T varies between 0.1 and 0.7. **(f)** Close-up of (e). **(g)** Gap pressure $P = P^{-}$ vs X as T varies.

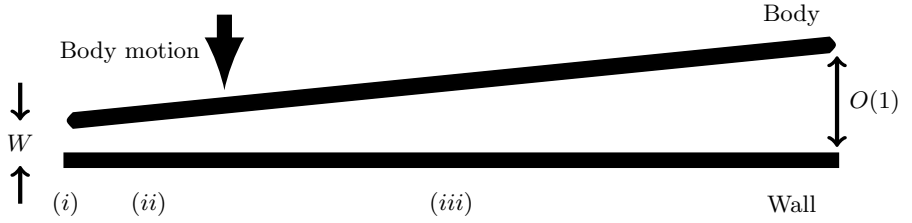

Figure 3: Sketch of the impact zones $(i) - (iii)$ induced during leading-edge impact of a flat plate. Here $W \ll 1$. The streamwise lengths of (i)-(iii) are of orders $W^2, W, 1$ respectively.

jump a to be of order unity in general. It is found that three zones $(i) - (iii)$ come in to operation within the gap, as sketched in Figure 3. Zone (i) occurs due to the $X^{1/2}$ growth in thickness of the Blasius-like layers near the leading edge becoming comparable with the $O(W)$ gap width, which indicates a short streamwise length scale of order W^2. Zone (ii) emerges where the X^n growth in gap width becomes of the same order as the small original gap width W and this points to a $W^{1/n}$ streamwise scaling. Zone (iii) has streamwise length of order unity and so covers the remainder of the gap, connecting with the trailing edge condition.

Zone (i) is the most upstream zone. Here the flow properties are nonlinear of viscous-inviscid form as the orders of magnitude involved lead to the expansion, for $X = W^2 x^*, Y = W y^*$,

$$U = u^*(x^*, y^*) + o(1), \quad P = p^*(x^*) + o(1), \quad \Psi = W\psi^*(x^*, y^*) + o(W). \tag{4.1}$$

This leads from (2.3a,b) to the boundary-layer equations holding in full within the present small zone,

$$u^* = \psi^*_{y^*}, \quad v^* = -\psi^*_{x^*}, \quad u^* u^*_{x^*} + v^* u^*_{y^*} = -p^{*\prime}(x^*) + u^*_{y^* y^*}, \tag{4.2a}$$

subject to the boundary conditions:

$$u^* = (a + U_w) \text{ at } x^* = 0^+, \tag{4.2b}$$

$$u^* = U_w, \; v^* = 0 \text{ at } y^* = 0, \tag{4.2c}$$

$$u^* = v^* = 0 \; (\psi^* = a + U_w) \text{ at } y^* = 1. \tag{4.2d}$$

The underbody shape acts here as a horizontal flat plate because the streamwise length scale is quite small. Similarly the influence of the incident shear λ is negligible at leading order because the normal length scale is small, such that the dominant flow is affected only by the initial velocity profile $(a + U_w)$ corresponding to uniform incident flow. The latter confirms the presence of Blasius-like behaviour at small x^* on both of the effective walls $y^* = 0, 1$. We show in Figure 4(a-f) numerical solutions of the nonlinear system (4.2a-d) based on our previous scheme. In these solutions U_w is set to unity without loss of generality and the value of the jump term a (or more generally a/U_w) is varied. When $a = 1$ the scaled wall shear stresses WSS, i.e. τ^*_g, τ^*_b, remain positive throughout and the pressure gradient is favourable as indicated in Figure 4(a). The constriction effect and accompanying favourable pressure gradient close to the leading edge are again observed, while downstream the stresses and pressure gradient become almost constant. The velocity profiles in Figure 4(b) highlight the change from undeveloped to developed flow as fluid passes downstream, indicating a comparatively rapid approach to an asymptotic form as x^* increases (velocity profiles are shown at x^* values of

$0.015, 0.061, 0.139, 0.248$, with the last two here being virtually indistinguishable). The results for the stresses, pressure gradients and profiles in Figures 4(c,d) for $a = 0$ and 4(e,f) for $a = -0.7$ show that the trends continue but with a small portion of reversed flow appearing at the underbody as the stress there changes sign and the pressure gradient becomes slightly adverse. It is notable that the solution is nontrivial even for zero a because of the underbody condition on the total mass flux.

Downstream at large x^* we anticipate from the equations and from the numerical solutions that the following response applies,

$$u^* \to O(1), \quad u^*_{y^*y^*} \to O(1), \text{ pressure gradient } p^{*\prime}(x*) \to O(1), \text{ as } x^* \to \infty. \quad (4.3a)$$

with inertial forces becoming comparatively small and the flow thus tending towards a lubrication dominance. This last leads to a combination of Poiseuille and Couette flow. In detail, and supposing a to be $O(1)$ but probably not equal to $-U_w/2$, let us guess that $p^{*\prime}(x^*)$ tends to a nonzero constant q^* say: in many cases we might expect q^* to be negative, giving a favourable pressure gradient. Solving (4.2a, c, d) without the inertial terms gives:

$$u^* \to \frac{1}{2}q^*({y^*}^2 - y^*) + U_w(1 - y^*) \text{ as } x^* \to \infty. \quad (4.3b)$$

Then mass conservation from (4.2d) relates the jump term a and the pressure gradient q^* in the form:

$$a = -\frac{U_w}{2} - \frac{q^*}{12}. \quad (4.3c)$$

This downstream flow is attached if $q^* < 2U_w$, with the wall shear at the top wall then being positive, but it is reversed if the induced pressure gradient is so adverse that $q^* > 2U_w$. The pressure p^* tends linearly to $\pm\infty$ like q^*x^*. The analytical predictions here agree with the trends in the numerical solutions of Figure 4(a-f) as a/U_w is varied.

Zone (ii) comes next downstream. Here $X = W^{1/n}x^{**}, P = W^{1/n-2}p^{**}$, $\Psi = W\psi^{**}$, $U = u^{**}$ and lubrication effects are paramount, yielding the reduced form:

$$u^{**} = \psi^{**}_{y^*}, \qquad v^{**} = -\psi^{**}_{x^{**}}, \qquad 0 = -p^{**\prime}(x^{**}) + u^{**}_{y^*y^*}, \quad (4.4a)$$

after substitution into (2.3a, b). The shape or gap width is WF^{**} where $F^{**} = 1+\gamma {x^{**}}^n$. We find the solution:

$$\frac{dp^{**}}{dx^{**}} = \frac{12(\frac{1}{2}U_wF^{**} - (a + U_w))}{{F^{**}}^3}. \quad (4.4b)$$

As a check on the matching, as x^{**} tends to 0^+ we obtain $dp^{**}/dx^{**} \to q^*$ as required, given that the scaled shape F^{**} tends to 1 then. Further, integrating (4.4b) gives

$$p^{**}(x^{**}) = p^{**}(0) + 12\int_0^{x^{**}} \frac{\frac{1}{2}U_wF^{**} - (a + U_w)}{{F^{**}}^3}dx^{**}, \quad (4.4c)$$

where matching with (4.3a-c) yields $p^{**}(0) = 0$. Further downstream, we expect in anticipation of the Kutta condition (which is relatively far away) and matching that the condition

$$p^{**}(\infty) = 0, \quad (4.4d)$$

is required. This leads to the balance:

$$\frac{1}{2}U_w\int_0^{\infty} \frac{1}{{F^{**}}^2}dx^{**} = (a + U_w)\int_0^{\infty} \frac{1}{{F^{**}}^3}dx^{**}. \quad (4.4e)$$

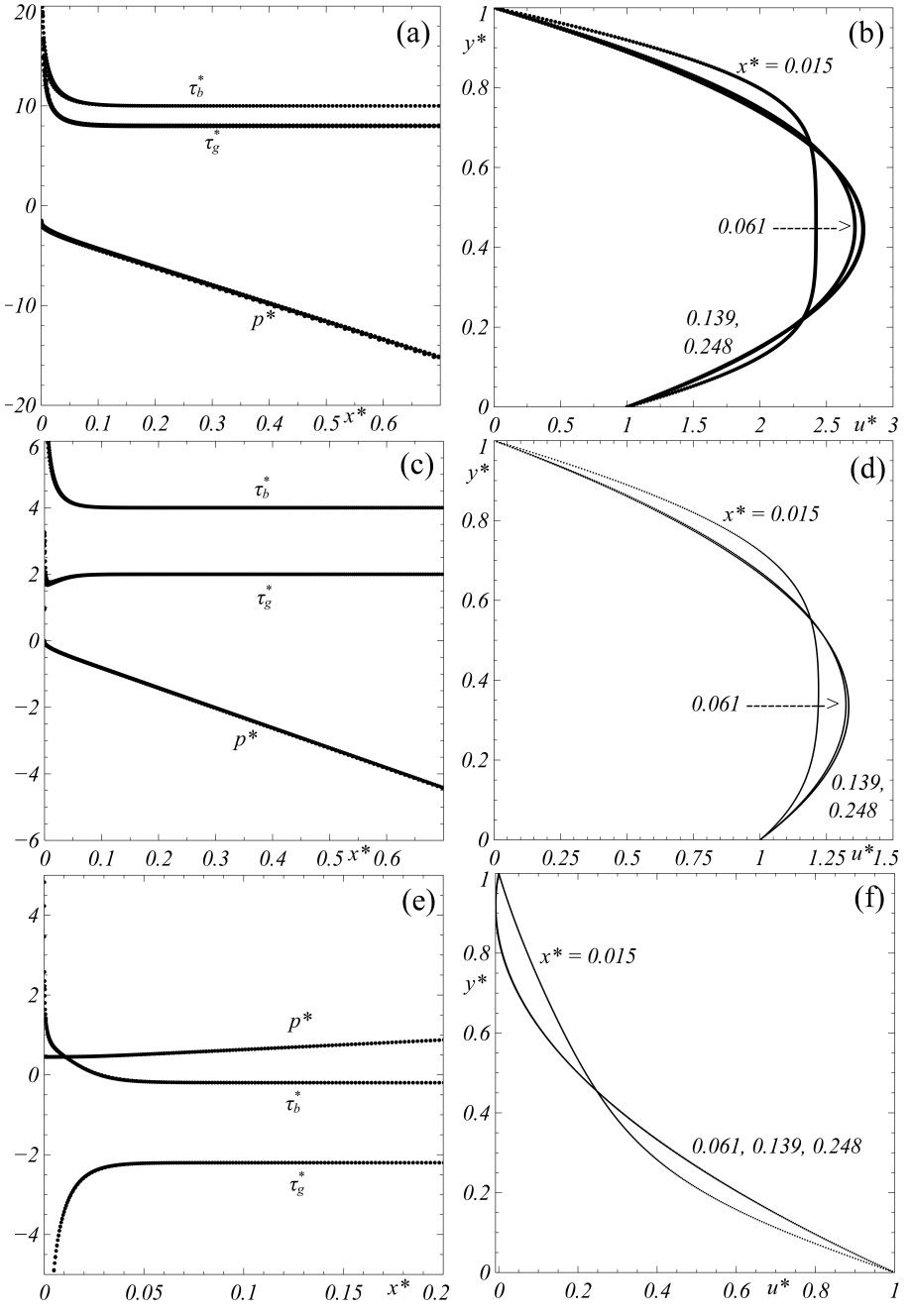

Figure 4: Solution of the zone (i) problem in leading-edge impact. **(a, b)** WSS, pressure development and velocity profiles when $a = 1$. **(c, d)** as (a, b) but $a = 0$. **(e, f)** as (a, b) but $a = -0.7$. Here $U_w = 1$ throughout. The velocity profiles are presented at four stations $x^* = 0.015, 0.061, 0.139, 0.248$; we remark that some of the profiles at the larger x^* values here are almost identical. Here the power n in the under-shape is arbitrary.

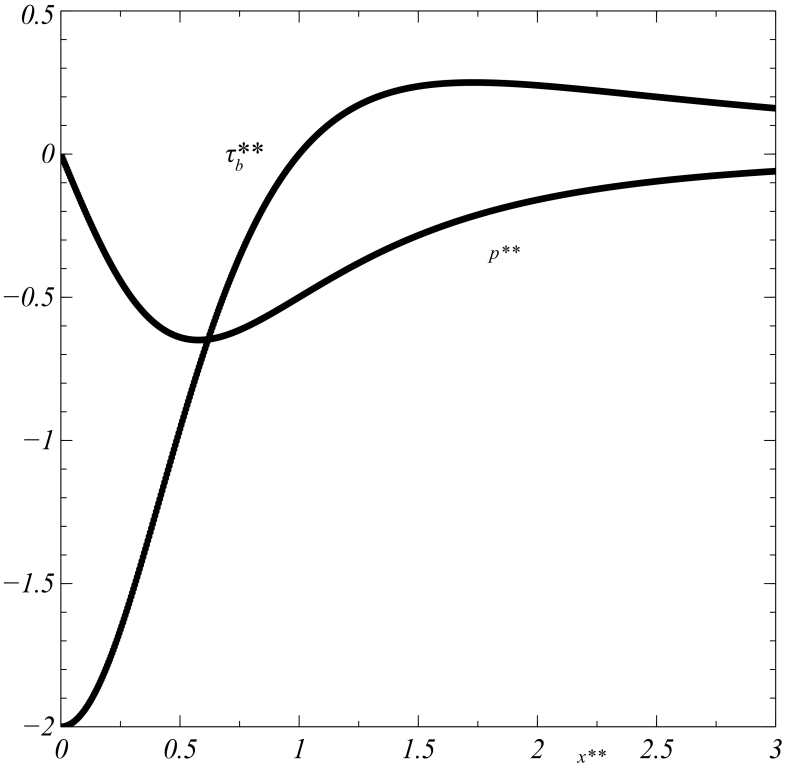

Figure 5: Pressure solution and scaled WSS (τ_b) at underbody in zone (ii) of a leading-edge impact. Here power n is unity.

This serves to determine a in terms of U_w and hence we can deduce q^* from (4.3c), contributing the simple forms

$$a = -\frac{(n-1)U_w}{2n-1}, \quad q^* = \frac{-6U_w}{2n-1}. \tag{4.4f}$$

We note that $n > 1/2$, implying that the effective pressure gradient q^* is always favourable when U_w is positive. Then the pressure solution p^{**} follows from (4.4c): see Figure 5 which shows p^{**} and the scaled WSS at the underbody surface, τ_b^{**}. That wall shear is found to reverse at the position where $F^{**} = 3n/(2n-1)$. This is a passive reversal since the flow here is a lubrication flow. We notice in addition that the constant term a is zero for the prime case $n = 1$ of the flat plate.

Comparisons can be made with the computational study in Jones & Smith (2003) of a ground-effects model for automobile undercarriages. Concerning comparison with their case where $n = 1$ and $\gamma = 1$, $h = W = 1/4$, the result of interest is in their Figure 2b's bottom left-hand corner. They find separation at an x^{**} value very close to $1/2$, from their τ_b plot. Our analysis for small W, with n set to unity, predicts separation at $x^{**} = x^{**}_{\rm sep}$ such that:

$$x^{**}_{\rm sep} = \left(\frac{W}{\gamma}\right)^{\frac{1}{2}}, \tag{4.5}$$

which gives 1/2 exactly in that case. In addition the trends in the present solutions for the scaled quantities p^{**}, τ_{ub}^{**} in Figure 5 agree well with those in Jones & Smith (2003)'s Figures 2a, 2b where (γ, W) are (16, 1) and (1, 0.25) respectively.

The pressure asymptote in zone (ii) as $x^{**} \to \infty$ needs stating here. It is

$$p^{**} = \frac{6\gamma^{-2}U_w}{1-2n} x^{**\,1-2n} + ..., \tag{4.6}$$

from (4.4c) combined with the requirement (4.4e).

Zone (*iii*) is the final zone and covers the majority of the gap. Here X, Y and the velocities and pressure are all of $O(1)$, owing to the behaviour in (4.6), and so the solution expands in the form

$$(U, V, \Psi, P) = (\hat{u}, \hat{v}, \hat{\psi}, \hat{p}) + ... \, . \tag{4.7}$$

Hence from (2.3a, b) we again have the full nonlinear equations holding,

$$\hat{u} = \hat{\psi}_Y, \quad \hat{v} = -\hat{\psi}_X, \quad \hat{u}\hat{u}_X + \hat{v}\hat{u}_Y = -\hat{p}'(X) + \hat{u}_{YY}, \tag{4.8a}$$

but subject to the constraints

$$\hat{u} = U_w, \ \hat{v} = 0 \ (\hat{\psi} = 0) \text{ at } Y = 0, \tag{4.8b}$$

$$\hat{u} = \hat{v} = 0 \ (\hat{\psi} = 0) \text{ at } Y = F(X). \tag{4.8c}$$

The total mass flux in zone (*iii*) is zero, which is due physically to the near-closure of the gap in zone (*ii*) and means that reversed flow must persist in zone (*iii*) throughout the interval of interest here, namely $0 < X < 1$. The near-closure at the upstream end of the current zone is also reflected in the fact that in this zone the representative shape has

$$F(X) = \gamma X^n \text{ for } 0 < X < 1, \tag{4.8d}$$

thus tending to zero (closure) at the origin. Matching requires that the pressure response is singular in the form

$$\hat{p} \sim \frac{6\gamma^{-2}U_w}{1-2n} X^{1-2n} + ... \text{ as } X \to 0^+, \tag{4.8e}$$

in view of (4.6), the velocity and mass-flux properties associated locally with (4.8e) being those of plane Poiseuille flow and Couette flow near the origin, from substitution of (4.8d,e) into (4.8a-c). At the other end, joining to the upper flow via the Kutta condition needs careful argument as per the Jones & Smith (2003) description, although we can set $\hat{p}$ to zero at the trailing edge without loss of generality by subtracting a constant from the pressure at all X values. We note further that the upstream influence from reversed flow is often focussed over a relatively short distance (Smith (1984) and see Appendix B) because of the large eigenvalues involved and the simulations with separated flow given in Palmer & Smith (2020) also support the same trend.

The nonlinear problem (4.8a-e) is a numerical one in general. The special case where $n \to 1/2^+$ does admit an interesting nonlinear similarity solution (see Appendix A) where upstream influence from the Kutta condition acts only over a comparatively short length scale as described above. Moreover the case of small γ, which is in effect one of low amplitudes, allows a lubrication solution to hold throughout zone (*iii*) subject to the proviso in the last sentence: this is related to the mild separations encountered in the full time-marching computations of Figures 2. Otherwise computations are necessary. We proceeded with an iterative method which is described in Appendix B. Results are presented in Figure 6(a,b) showing respectively the streamwise velocity profiles

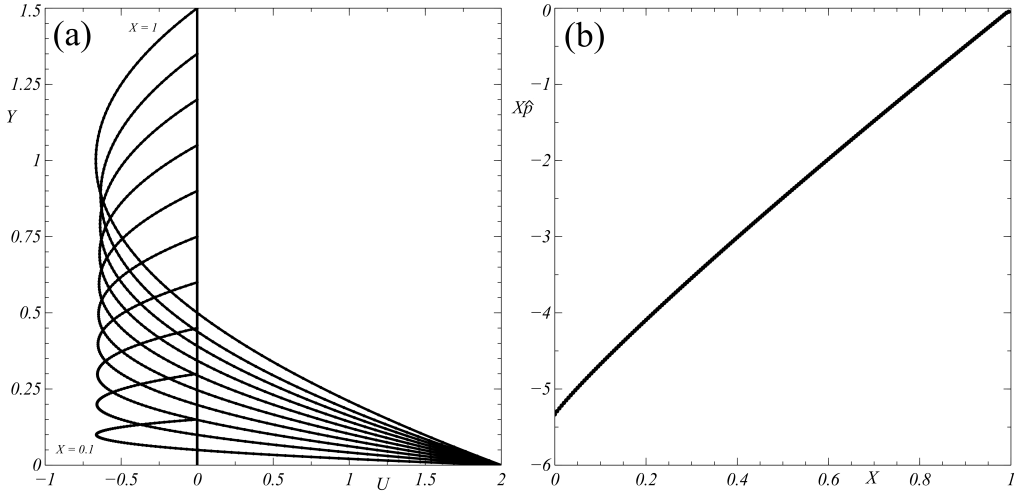

Figure 6: Solution for zone (iii) in leading-edge impact. (a) Velocity profiles. (b) Scaled pressure. Here power n is unity.

at successive stations, with flow reversal present at all stations in keeping with the requirement of zero total flux, and the pressure response which gives an adverse pressure gradient throughout. The profiles in this case appear nearly, but are not quite, similar: see also the description provided in the next subsection for the flow solutions in Figure 7(a,b). The results confirm that separated flow occurs throughout this viscous-inviscid area downstream of the contact area.

Relating the above findings to the original unsteady problem follows from the positive or negative pressure contributions in zones $(i) - (iii)$ to the scaled lift C_L and moment C_M in (2.7a,b). The C_L contribution from (i) is $O(W^2)$ and hence negligible since W is small, while the contribution from zone (ii) is $O(W^{2/n-2})$ and that from (iii) is $O(1)$; the same scales apply to the moment contributions. The contributions in (ii) are thus negligible when the power factor $n < 1$ but of order unity for the flat-plate case $n = 1$; also they are of relatively little interest here when $n > 1$ since then the body shape, being concave upwards, is in a marginal state with both the leading edge position and the slope of the curved body at the leading edge being zero then, which is a special case. In consequence the main normal force and moment on the body are of order unity and are, for this flat-plate case, produced by the lubrication-like zone (ii) and the inertial zone (iii) equally in terms of orders of magnitude. Further, the body-motion balances (2.7a,b) then imply that the effective accelerations $d^2h/dT^2, d^2\theta/dT^2$, whether positive or negative, are of $O(1)$ and hence the body velocities must be finite on approach to impact. The inferred form

$$W(T) \propto (T_0 - T) \tag{4.9}$$

therefore describes the behaviour of the leading-edge gap width at the onset of impact.

4.2. *Downstream-moving bodies*

All cases so far have been for an upstream-moving body. For generality we consider now the downstream-moving scenario which is associated of course with the wall moving upstream relative to the body in the current coordinate system. Certain aspects for a downstream-moving body are addressed in the similarity solution of Appendix A.

A computation of the flow in the long zone (iii) for the flat-plate shape with a

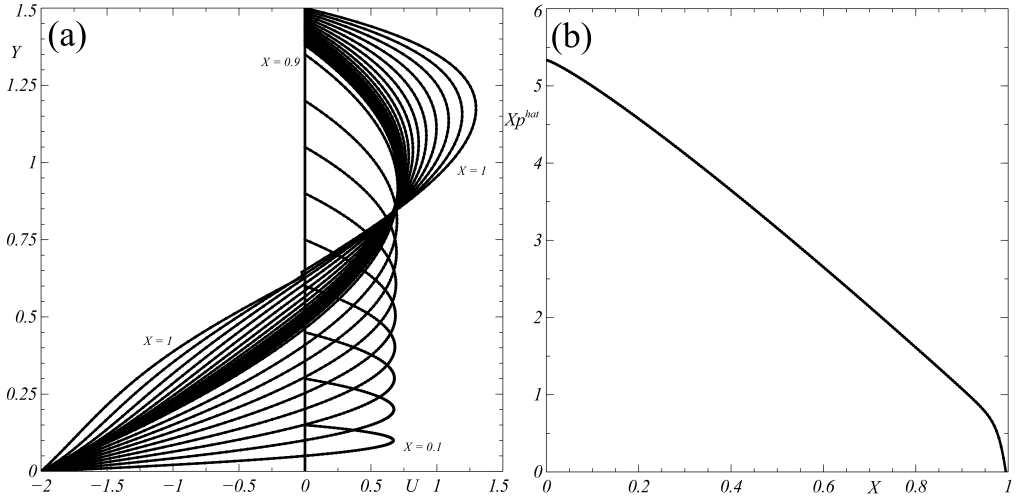

Figure 7: (a, b) As in Figure 6 but with the body translating downstream relative to the wall. Here power n is unity.

downstream body translation is shown in Figure 7(a,b), when impact occurs at the leading edge. Figure 7(a,b) presents in turn the velocity profiles at various stations and the pressure-gradient response which is here favourable throughout. Flow reversal is present at all stations in this viscous-inviscid area downstream of the effective contact at the leading edge. Although the velocity profiles in much of the flow field ahead of the trailing edge are broadly similar to each other, they change appreciably near the trailing edge of the domain, an aspect which occurs likewise in the findings of Figure 6(a) as well as in the separated wake profiles described in Palmer & Smith (2020). Moreover, the solution presented in Figure 7(a, b) is nearly the same as that in a trailing-edge impact for an upstream-moving body (mentioned at the end of section 3).

5. Comparisons with direct numerical simulations of the Navier-Stokes equations

Comparisons may now be considered between the present asymptotic predictions of flow properties and the direct numerical simulation results for steady flow in Palmer & Smith (2020) over a range of finite Reynolds numbers.

As remarked at the end of section 2 the present interaction can be expressed broadly in terms of the local incident shear value as in Palmer & Smith (2020) as well as in the current specific context of a surrounding boundary layer motion. The relation between the Reynolds numbers involved in the two contexts is

$$R = O\left(\ell^2 Re^{3/2}\right), \tag{5.1}$$

where Re is the globally based Reynolds number of the present work and R is a local shear-based Reynolds number as in Palmer & Smith (2020). Thus the lower restriction on the body length ℓ in (2.1) corresponds to the value of R being large. It can be shown that the formulation for large R in Palmer & Smith (2020) tends consistently to the present condensed-flow formulation of (2.3a)-(2.5c) as R increases. This trend also includes the Euler formulation having zero displacement as in the flow solutions of Smith & Servini (2019).

The simulation work in Palmer & Smith (2020) shows that the flow past a thin flat-plate body can readily separate when the body is sufficiently close to the wall, whether inclined or not, and that a substantial wake then exists. Also, the upstream influence is observed to decrease in terms of its length scale as the Reynolds number is increased for cases of non-negative wall velocity, i.e. for a body which is either stationary or translating upstream relative to the wall. The findings of the present analytical work agree on those three aspects concerning separation, wake effect and upstream influence. The enhanced wake effect is mainly a consequence of the enhanced distortion of the velocity profiles at the trailing edge according to the solutions in sections 3, 4 and Appendix A, whereas the decreased extent of upstream influence is due to the flow response being focussed in the comparatively small Euler region around the leading edge of the body.

The results in Palmer & Smith (2020) also indicate the presence of zones of rapid spatial variation in the streamwise pressure gradient beneath the body as the Reynolds number increases and/or the gap width is reduced. The velocity profiles likewise display sensitive behaviour as the gap width decreases, giving jet-like forms at some finite gap widths but ultimately flow reversal at the smallest widths for the cases of non-negative wall velocity whereas interesting opposing-flow characteristics are present when the wall velocity is negative: see also the present Appendix A. These and other comparisons show there is significant qualitative agreement between the two works. In addition there is quantitative agreement since the scales in the present paper are consistent with the computational trends of Palmer & Smith (2020), for example on the pressure variation. When R increases the central case addressed in Palmer & Smith (2020) has the gap-width scale being of order $R^{-1/3}$ with the streamwise velocity component and the pressure scaling as $-1/3$ and $-2/3$ powers respectively, in keeping with the scalings in (2.2). The simulation study finds the scaled pressure then tends (see Table 1 in Palmer & Smith (2020)) quite convincingly to a constant as the Reynolds number is increased. This is in agreement with the present asymptotic theory.

6. Further discussion

A major thrust of the study has been on understanding the influences of physical scales, nonlinear effects, initial conditions and parametric effects on impact of a thin body onto a solid wall and the accompanying flow separations. Our interest has been in substantial two-way coupling between the body motion and the fluid flow around it within a wall layer. This involves in particular inertial effects, significant regions of flow reversals and the nonlinear dynamics of viscous-inviscid fluid motions as well as unusual flow structures during impacts upon the wall. The occurrence of three spatial zones, a nonlinear viscous-inviscid one followed by a viscous one and then another viscous-inviscid one, is most notable. Lubrication effects are important very close to the impact station, for sure, although the nonlinear-linear-nonlinear balance always applies by virtue of the three zones above. The ensuing lift and moment on the body which help control the body movement near impact are due, at leading order, to contributions from two of the three zones in the present case of a flat-plate body. All of these impacts take place within a finite scaled time and produce flow reversals inside the thin gap between the body and the wall owing to the shrinkage of the mass flux to zero in the gap.

The comparisons between the predictions of the asymptotic analysis given in the present paper and the steady-flow results of direct numerical simulations in Palmer & Smith (2020) tend to be affirmative in respect to agreement on the trends as Reynolds numbers increase; see section 5. Quantitative agreement to within 20 per cent in the gap pressure is typically found for local Reynolds numbers above about 100. This corresponds

to a rather wide range of global Reynolds numbers and body lengths. The comparisons also support the considerable role of the Euler region near the leading edge. Comparisons for other body shapes and orientations could well be of interest.

There is likely to be significant dependence on body shape as well as on the initial conditions of the body position and velocity. These affect whether leading-edge, trailing-edge or mid-chord impact arises or indeed whether the body can move in the normal direction away from the wall instead. There is also dependence on the streamwise translation of the body. We have addressed upstream translation mostly but the impact analysis and allied computations suggest that essentially the same characteristics apply for a downstream translation of the body, while the non-translating case is felt likely to bring the incident shear flow back into influence near the onset point of impact. See also the simulations for translating or stationary bodies in Palmer & Smith (2020). It is interesting that in the scenario of downstream translation the role of the leading and trailing edges can interchange particularly at impact; flow separation can similarly cause a leading edge to act as a trailing edge and vice-versa in effect. Further influence rests with other parametric effects some of which remain to be studied. The influence of large body mass and moment of inertia is to make the normal velocity and rotation of the body nominally uniform which, according to the impact analysis, is consistent with the finite-time termination described here. The flow length, time, pressure and velocity scales as well as the length, mass and moment of inertia scales of the body are also of interest both at the initiation stage and at the termination due to impact.

Issues for future study are many. A wider range of body shapes needs investigating for example. On a broader scope, three-dimensional bodies, more unsteady flows and multi-body interactions are of concern, depending on the application in mind. More narrowly and immediately perhaps, it would be interesting to take the current study further on in time into shorter time scales during impact and then beyond those. The present work has far from answered all prospective questions in the area. The body could fly out of the wall layer away from the wall by the interactions present and indeed some numerical cases (not shown here) are able to fly away from the wall in that manner. Since shapes are very varied in reality more details of trailing-edge and mid-chord impacts may be called for eventually, in particular concerning trailing-edge separations and upstream influence (Smith 1984; Jones & Smith 2003). Flexible bodies are of relevance in several application areas, an aspect which would be interesting to connect with the current scaled nonlinear interaction. Longer bodies tend to lead to simplifications in the flow response on top of the body in the boundary-layer setting, for example as in Smith & Palmer (2019)'s inviscid account for body velocities of the order of the freestream speed, and hence alterations to the present fluid-body interaction. The relation between these cases and the termination behaviour found here remains unknown. Finally here, the zero net flux seen at impact is potentially relevant to certain near-wall devices such as hinged mounted flaps.

Acknowledgements

Thanks are due to personnel at AeroTex (Richard Moser, Ian Roberts, Colin Hatch) for their interest in the area, to EPSRC through grants EP/R511638/1, GR/T11364/01, EP/G501831/1, EP/H501665/1, EP/K032208/1 during part of this research, to EPSRC /IAA and AeroTex for support of RP, and to Alric Rothmayer for helpful discussion of a number of related points. The referees are thanked for their very helpful comments.

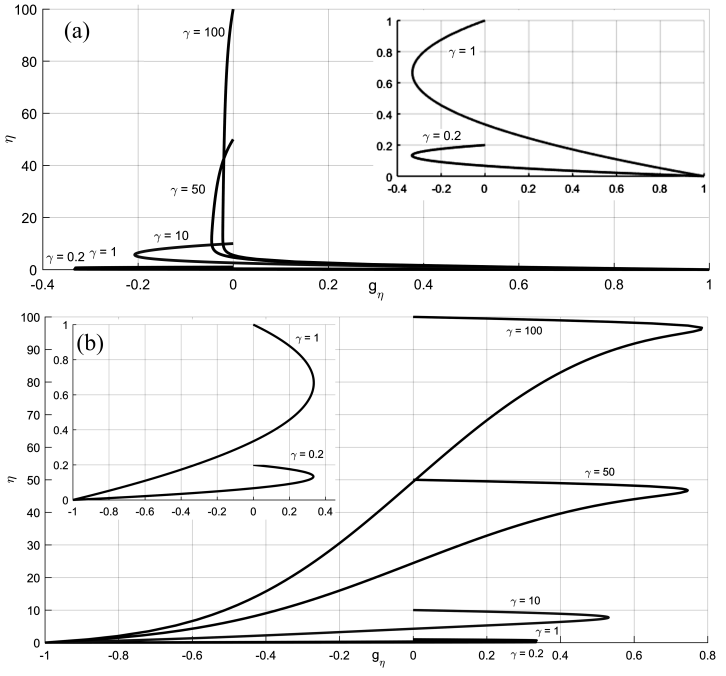

Figure 8: Nonlinear similarity solutions in Appendix A. Scaled velocity profiles $dg/d\eta$ for (a) $U_w = 1$, (b) $U_w = -1$.

Declaration of Interests

The authors report no conflict of interest.

Appendix A. Nonlinear similarity solutions

Similarity properties arise for the underbody shapes $F(X) = \gamma X^n$, where $0 < X < 1$, in zone (iii) of section 4 for a body translating upstream relative to the lower wall in the limit as n tends to $1/2$ and likewise when the body is translating downstream. (Zones (i), (ii) merge when n tends to $1/2$ into a single zone in which X, Y have orders W^2, W in turn and the boundary layer equations hold in full.) The properties here also have connections with the study in Palmer & Smith (2020). The formal expression involved has

$$[\hat{u}, \hat{\psi}, \hat{p}] = [g'(\eta), X^{1/2} g(\eta), \ln(X) P_1], \quad y = X^{1/2}\eta, \tag{A 1}$$

where the prime notation denotes differentiation with respect to η and the similarity function $g(\eta)$ and pressure coefficient P_1 are to be found. The nonlinear governing equation from (4.8a) is

$$g''' + \frac{1}{2} g g'' = P_1 \tag{A 2}$$

and the boundary conditions require

$$g(0) = 0, \quad g'(0) = U_w, \quad g(\gamma) = g'(\gamma) = 0. \tag{A 3}$$

Computed solutions are presented in Figure 8(a,b) with, respectively, U_w being ± 1 without loss of generality: upstream and downstream movement of the body corresponds to U_w equal to ± 1 respectively.

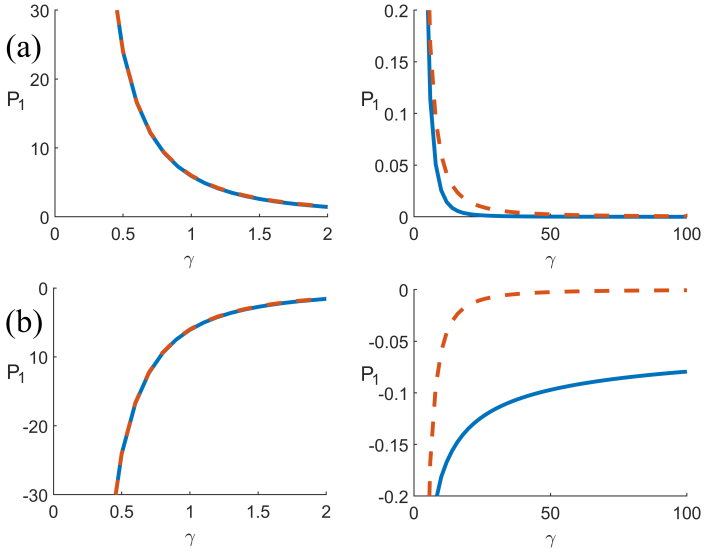

Figure 9: The pressure coefficient P_1 vs γ (from Appendix A) when (a) $U_w = 1$, (b) $U_w = -1$. The dashed curves show asymptotes for small γ for comparison.

The plots in Figure 8(a,b) show the scaled velocity profiles $g'(\eta)$ as the value of γ is varied. The corresponding results for the pressure term P_1 versus γ are given in Figure 9(a, b). Virtually all the solutions indicate that P_1 is positive for positive U_w and negative for negative U_w. In the case of an upstream-moving body when γ is small the nonlinear terms in (A2) are negligible, as in a lubrication effect, and analytical expressions are available which are seen to agree well with the numerical solutions. When γ becomes large the bulk of the gap flow becomes quasi-inviscid with $O(\gamma)$ thickness and the flow solution g becomes almost linear there whereas the viscous-inviscid wall layer adjoining $\eta = 0$ is only of $O(1)$ thickness and yields a wall-jet effect. Similar behaviour occurs for the case of the downstream-moving body apart from the viscous-inviscid wall layer being forced to the underbody surface $\eta = 1$ when γ is large.

Appendix B. Treatment of long zones

This concerns the nonlinear long zone (*iii*) in the scenario of leading-edge impact addressed in section 4. We concentrate on the flat-plate shape $n = 1$ because of the focus on that case in the time-marching computations. At the trailing-edge station the streamwise velocity profile is expected to give incoming flow (u negative) in the upper part of the profile and outgoing flow (u positive) below that, as confirmed in Palmer & Smith (2020), since the lower wall is moving downstream and yet zero mass flux is required across the gap. Strictly the incoming flow dictates over the outgoing flow as the governing equations are parabolic in the flow direction but this is affected also by the lateral boundary conditions on the gap walls. Given the singular behaviour (4.8e) we set

$$[\hat{u}, \hat{\psi}, \hat{p}] = [\bar{u}, X\bar{\psi}, X^{-1}\bar{p}], \quad Y = X\bar{y}, \tag{B 1}$$

in order to work with O(1) variables. Hence the governing equations and boundary conditions become

$$\bar{u} = \bar{\psi}_{\bar{y}}, \quad X^2(\bar{u}\bar{u}_X - \bar{\psi}_X\bar{u}_{\bar{y}}) - X\bar{\psi}\bar{u}_{\bar{y}} = \bar{p} - X\bar{p}_X + \bar{u}_{\bar{y}\bar{y}}, \tag{B 2}$$

subject to

$$\bar{u} = U_w, \bar{v} = 0 \ (\bar{\psi} = 0) \text{ at } \bar{y} = 0; \quad \bar{u} = \bar{v} = 0 \ (\bar{\psi} = 0) \text{ at } \bar{y} = \gamma, \tag{B 3}$$

$$\bar{u} \to O(1), \quad \bar{\psi} \to O(1), \quad \bar{p} \to -6\gamma^{-2}u_w + ... \text{ as } X \to 0^+, \tag{B 4}$$

with (B4) indicating that the end constraints on $\bar{u}, \bar{\psi}, \bar{p}$ are specific and finite. Here $\bar{v} = -X\bar{\psi}_X - \bar{\psi} + \bar{y}\bar{u}$. In fact

$$\bar{u}(0^+, \bar{y}) = U_w(3\gamma^{-2}\bar{y} - 1)(\gamma^{-2}\bar{y} - 1). \tag{B 5}$$

The other end condition is effectively the Kutta one on pressure but supplemented by the reversed flow part $\bar{u}_{TE}(\bar{y})$ of the flow-velocity profile at the trailing edge,

$$\bar{p} = 0, \quad \bar{u} = \bar{u}_{TE}(\bar{y}) \ (y_1 < \bar{y} < \gamma) \text{ at } X = 1^-. \tag{B 6}$$

Here y_1 is the $\bar{y}$ location of the dividing streamline at the trailing-edge station.

We treated the system (B2-B6) by iterating from the low amplitude solution, i.e. by means of iterations of the form

$$[\bar{u}_{\bar{y}\bar{y}} + \bar{p} - X\bar{p}_X]^{(m)} = \left[X^2(\bar{u}\bar{u}_X - \bar{\psi}_X\bar{u}_{\bar{y}}) - X\bar{\psi}\bar{u}_{\bar{y}}\right]^{(m-1)}. \tag{B 7}$$

Here (m) denotes the iteration number, $m = 1, 2, ...$, and the zero-th solution is taken to be the lubrication one where the right-hand side in (B7) is negligible. This approach was taken in order to treat the whole flow problem in a more elliptic manner in view of the reversed flow expected at every streamwise station. Each iteration involves triple integration in $\bar{y}$ to determine updated $\bar{u}, \bar{\psi}$ fields, integration in X to find new $\bar{p}$ values, followed by differentiation in X to update the right-hand sides. The discretised version of this differentiation makes use of windward differencing and thus incorporates effects from the reversed flow profile in (B6). The approach here is consistent with that of Jones & Smith (2003) who also computed the wake solution. The iterations are continued until successive iterates in $\bar{p}$ differ by less than a small tolerance, typically 10^{-6}, at each X station. As a check on accuracy our results were found to be in close agreement with those obtained from the different numerical approach by Jones & Smith (2003) in their Figure 2 for a particular wedge-like shape with small mass flux and separated flow present.

REFERENCES

Anderson, D., Tannehill, J. C. & Pletcher, R. H. 2016 *Computational fluid mechanics and heat transfer*. CRC Press.

Dehghan, M. & Basirat Tabrizi, H. 2014 Effects of coupling on turbulent gas-particle boundary layer flows at borderline volume fractions using kinetic theory. *Journal of Heat and Mass Transfer Research* **1** (1), 1–8.

Einav, S. & Lee, S. L. 1973 Particles migration in laminar boundary layer flow. *International Journal of Multiphase Flow* **1** (1), 73–88.

Gent, R. W., Dart, N. P. & Cansdale, J. T. 2000 Aircraft icing. *Philosophical Transactions of the Royal Society of London. Series A: Mathematical, Physical and Engineering Sciences* **358** (1776), 2873–2911.

Hall, G. R. 1964 On the mechanics of transition produced by particles passing through an initially laminar boundary layer and the estimated effect on the LFC performance of the X-21 aircraft. *Tech. Rep.*. NASA.

Jones, M. A. & Smith, F.T. 2003 Fluid motion for car undertrays in ground effect. *Journal of Engineering Mathematics* **45** (3-4), 309–334.

Kishore, N. & Gu, S. 2010 Wall effects on flow and drag phenomena of spheroid particles at moderate reynolds numbers. *Industrial & Engineering Chemistry Research* **49** (19), 9486–9495.

Loisel, V., Abbas, M., Masbernat, O. & Climent, E. 2013 The effect of neutrally buoyant

finite-size particles on channel flows in the laminar-turbulent transition regime. *Physics of Fluids* **25** (12), 123304.

Loth, E. & Dorgan, A. J. 2009 An equation of motion for particles of finite Reynolds number and size. *Environmental Fluid Mechanics* **9** (2), 187–206.

Norde, Ellen 2017 *Eulerian method for ice crystal icing in turbofan engines*. University of Twente.

Palmer, R. A. & Smith, F. T. 2019 When a small thin two-dimensional body enters a viscous wall layer. *European Journal of Applied Mathematics* pp. 1–27.

Palmer, R. A. & Smith, F. T. 2020 A body in nonlinear near-wall shear flow: numerical results for a flat plate (under review). *Journal of Fluid Mechanics* .

Petrie, H. L., Morris, P. J., Bajwa, A. R. & Vincent, D. C. 1993 Transition induced by fixed and freely convecting spherical particles in laminar boundary layers. *Tech. Rep.*. Pennsylvania State University, University Park Applied Research Lab.

Poesio, P., Ooms, G., Ten Cate, A. & Hunt, J. C. R. 2006 Interaction and collisions between particles in a linear shear flow near a wall at low Reynolds number. *Journal of Fluid Mechanics* **555**, 113–130.

Portela, L. M., Cota, P. & Oliemans, R. V. A. 2002 Numerical study of the near-wall behaviour of particles in turbulent pipe flows. *Powder Technology* **125** (2-3), 149–157.

Purvis, R. & Smith, F. T. 2016 Improving aircraft safety in icing conditions. In *UK Success Stories in Industrial Mathematics*, pp. 145–151. Springer.

Schmidt, C. & Young, T. 2009 Impact of freely suspended particles on laminar boundary layers. In *47th AIAA Aerospace Sciences Meeting including The New Horizons Forum and Aerospace Exposition*, p. 1621.

Smith, F. T. 1976 Flow through constricted or dilated pipes and channels: Part 2. *The Quarterly Journal of Mechanics and Applied Mathematics* **29** (3), 365–376.

Smith, F. T. 1984 Concerning upstream influence in separating boundary layers and downstream influence in channel flow. *The Quarterly Journal of Mechanics and Applied Mathematics* **37** (3), 389–399.

Smith, F. T. 2017 Free motion of a body in a boundary layer or channel flow. *Journal of Fluid Mechanics* **813**, 279–300.

Smith, F. T. & Daniels, P. G. 1981 Removal of Goldstein's singularity at separation, in flow past obstacles in wall layers. *Journal of Fluid Mechanics* **110**, 1–37.

Smith, F. T. & Ellis, A. S. 2010 On interaction between falling bodies and the surrounding fluid. *Mathematika* **56** (1), 140–168.

Smith, F. T. & Johnson, E. R. 2016 Movement of a finite body in channel flow. *Proceedings of the Royal Society A: Mathematical, Physical and Engineering Sciences* **472** (2191), 20160164.

Smith, F. T., Ovenden, N. C., Franke, P. T. & Doorly, D. J. 2003 What happens to pressure when a flow enters a side branch? *Journal of Fluid Mechanics* **479**, 231–258.

Smith, F. T. & Palmer, R. 2019 A freely moving body in a boundary layer: Nonlinear separated-flow effects. *Applied Ocean Research* **85**, 107–118.

Smith, F. T. & Servini, P. 2019 Channel Flow Past A Near-Wall Body. *The Quarterly Journal of Mechanics and Applied Mathematics* **72**, 359–385.

Smith, F. T. & Timoshin, S. N. 1996 Blade-wake interactions and rotary boundary layers. *Proceedings of the Royal Society of London. Series A: Mathematical, Physical and Engineering Sciences* **452** (1949), 1301–1329.

Wang, J. & Levy, E. K. 2006 Particle behavior in the turbulent boundary layer of a dilute gas-particle flow past a flat plate. *Experimental Thermal and Fluid Science* **30** (5), 473–483.

Yu, Z., Phan-Thien, N. & Tanner, R. I. 2007 Rotation of a spheroid in a Couette flow at moderate Reynolds numbers. *Physical Review E* **76** (2), 026310.